Interface and mechanical properties of the single-layer long fiber reinforced W_f/W composites fabricated via field assisted sintering technology

Rui Shu[a,b], Yiran Mao[a,d,*] , Jan W Coenen[a,e], Alexis Terra[a], Chao Liu[b], Stephan Schönen[f], Johann Riesch[c], Christian Linsmeier[a] and Christoph Broeckmann[b]

[a] *Forschungszentrum Jülich GmbH, Institut für Energie- und Klimaforschung - Plasmaphysik, Partner in the Trilateral Euregio Cluster, 52425 Jülich, Germany*

[b] *Institut für Werkstoffanwendungen im Maschinenbau (IWM), RWTH Aachen University, 52062 Aachen, Germany*

[c] *Max-Planck-Institut für Plasmaphysik, 85748 Garching b. München, Germany*

[d] *School of Mechanical Engineering, Hefei University of Technology, Hefei 230009, China*

[e] *Department of Engineering Physics, University of Wisconsin Madison, WI 53706 Madison, USA*

[f] *Forschungszentrum Jülich GmbH, Zentralinstitut für Engineering, Elektronik und Analytik - Engineering und Technologie (ZEA-1) , 52425 Jülich, Germany*

*Corresponding author: y.mao@fz-juelich.de (Yiran Mao).

Abstract: Tungsten fiber reinforced tungsten composites (W_f/W) show a pseudo-ductile behavior because of extrinsic toughening mechanisms such as interface de-bonding, pull-out and plastic deformation of the fiber. In the present work, single-layer long fiber W_f/W composites with and without yttrium oxide (Y_2O_3) interface were fabricated by a field assisted sintering technology (FAST) process. The microstructure and mechanical properties

of the prepared W_f/W composites were characterized. The fracture behavior and toughening mechanisms were analyzed in detail combining the results of experiments and finite element modelling. W_f/W composites with Y_2O_3 interface (weak interfacial strength) show a typical pseudo-ductile fracture behavior and a higher flexural strength than the composites without Y_2O_3 interface (strong interfacial strength). The fracture energy dissipation is mainly driven by plastic deformation of the fibers, but interface de-bonding is a necessary factor to ensure any extrinsic toughening mechanisms.

Keywords: Interface; Mechanical properties; Fracture mechanisms; W_f/W composites; Field assisted sintering technology.

1. Introduction

Due to its excellent properties with high temperature and plasma erosion resistance, Tungsten (W) is considered as the main candidate material for plasma-facing components in future fusion reactors [1–3]. However, a big challenge for its application is the intrinsic brittleness [4–7]. In order to improve the poor fracture toughness of tungsten, tungsten fiber reinforced tungsten (W_f/W) composites have been developed based on extrinsic toughing mechanisms [8–11].

At present, the main production routes are chemical vapor deposition (CVD) [12–15] and powder metallurgy (PM) [16–18]. It has been reported [19,20], CVD produced W_f/W represents typical pseudo-ductile behavior with significantly increased fracture toughness and fracture energy. The toughening mechanisms of fiber bridging, fiber necking and fiber pull out were observed [21]. However, W_f/W produced by CVD process is technically very complex with low reproducibility and high costs in terms of resources and time [2].

Compared with CVD process, PM production route has several benefits, such as substantial experience with bulk production, higher production rate and an easier realization of alloyed materials [17]. Mao et al. [22] prepared the W_f/W composites by field-assisted sintering technology (FAST, also known as spark plasma sintering, SPS) and hot isostatic pressing (HIP). Both composites have a similar microstructure of random and homogeneous fiber distribution with improved damage resilience because of the energy dissipation mechanisms of crack bridging and fiber pull-out. It has been reported [17], a relatively weak interface leads to a typical pseudo-ductile fracture behavior and shows a better toughening effect, while a strong interface is beneficial to achieve higher strength but weakens the pseudo-ductile behavior. Based on previous studies [23–26], the properties of the fiber-matrix interface have a great influence on the fracture behavior of fiber reinforced composites. The extrinsic toughening mechanism relies on the existence of the weak bonding between fiber and matrix (weak interface), either via a weak oxide interlayer [27] or porous connection [28] between fiber and matrix.

At present, all the W_f/W composites prepared by PM process are reinforced by randomly distributed short fibers. Compared to unidirectional long fiber reinforced composites, short fiber reinforced composites normally give limited toughening effect [29–32]. First of all, the strength of the randomly distributed short fiber W_f/W composite is relatively low. Due to the randomness of short fiber distribution, there will be a large number of fibers that are not well aligned with the given load. The weak interface of those fibers will suffer with tensile stress and fail before matrix failure, and act as defects (crack starting point) during loading. The crack propagation follows the pre-crack positions and those fibers will not contribute to the strength of composites, reducing the strength of the composites [17]. Secondly, the random

distribution of short fibers reinforced W_f/W composites has the problem of low fiber toughening efficiency, as there is no load transfer beyond the fiber ends [33]. Theoretical studies have shown that the efficiency of fiber toughening will increase as the length of the fiber increases. Compared with the abovementioned problems, the unidirectionally aligned long fibers can offer much higher toughening efficiency and material strength. It can be indicated by comparing the properties of the long fiber reinforced W_f/W composites of CVD [15] and short fiber reinforced W_f/W composites of PM [22]. The former shows higher strength and ductile behavior during the fracture process. The same goes for theoretical analysis.

Although many studies of FAST W_f/W composites have been reported [29,30], the theoretical study of the fracture mechanisms are restricted by the complexity of the random distributed short fibers. The contribution of each mechanism, i.e. interface de-bonding, fiber fracture etc., to the energy dissipation is not clear. At the same time, in order to achieve a suitable interface, yttrium oxide (Y_2O_3) is considered because of its good thermal and chemical stability and low activation due to neutron irradiation [34,35]. Y_2O_3 has been used as the interface layer of W_f/W composites and behaved well to improve the mechanical properties of W_f/W composites [15,18].

In this study, single layer long fiber reinforced W_f/W composites with and without Y_2O_3 interface between fibers and matrix were prepared by a FAST process. The influence of the interface properties on the strength, fracture behavior and toughening mechanisms were systematically analyzed and discussed. Based on the experimental results, numerical simulation based on extended finite element method (XFEM) was used to demonstrate the fracture process of the composites with different interfacial strength. This is the first time this

method has been applied in the context of PM W_f/W composites.

2. Experimental

2.1. W_f/W composite fabrication

The raw materials for the production are pure tungsten powders with an average particle size of 5 μm and tungsten weaves woven by W fibers [13]. The fibers are distributed unidirectionally in the warp direction with a distance of 0.2 mm, and the weft fibers with a small diameter (50 μm) and a large fiber distance (>5 mm) are mainly used to fix the warp fibers (150 μm). The production route of the single layer long fiber reinforced W_f/W composites is shown in Figure 1. The weaves were coated with an Y_2O_3 layer (with the thickness of ≈1.6 μm) by magnetron sputtering. The coating details are similar as described in Ref. [36]. Next, the W_f weaves (with and without Y_2O_3 respectively) and W powders were put into a graphite die (20 mm diameter) layer by layer. The thickness of W powder region between two W_f weaves is about 3 mm. The composite was consolidated via the FAST process, with a heating rate of 50 ℃/min and a holding time of 5 min at 1800 ℃ under 50 MPa. A commercial FAST system (HP D 25–2) from "FCT Systeme GmbH" (max force, 250 kN; max temperature, 2200 ℃; max heating rate, 400 K/min) is used in this study. The sintered W_f/W composite has 3 W_f layers and was subsequently cut into three single-layer long fiber reinforced W_f/W composite samples. The W_f/W composites without Y_2O_3 interface were also produced in a same process as the reference sample.

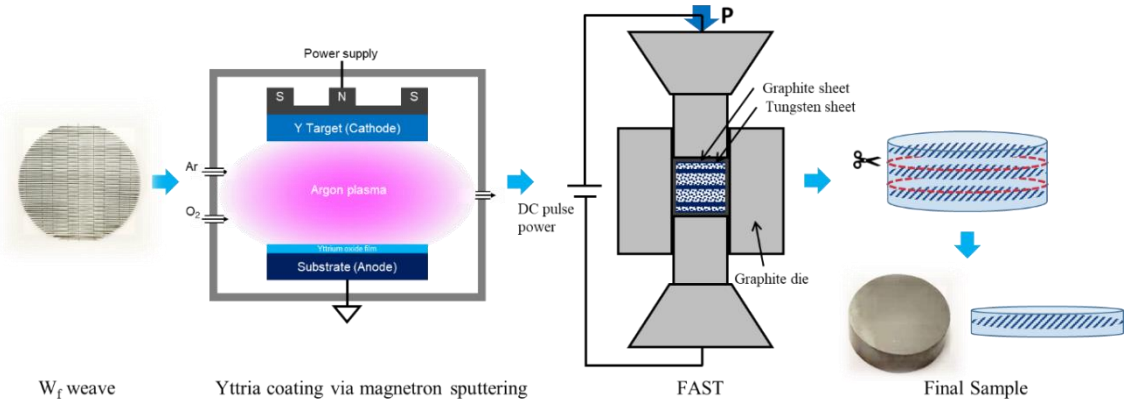

Figure 1. Schematic diagram of the preparation process of single-layer long fiber reinforced W_f/W composites

2.2. Characterization

The microstructure of the composite is analyzed via a LEO 982 scanning electron microscope (SEM) after mechanical polishing. The influence of the Y_2O_3 interface layer on the microstructure of the fibers is analyzed by a dual beam SEM/FIB (focused ion beam) Carl Zeiss Crossbeam 540 device.

To observe the fracture behavior, the composites is tested by 3-point bending test with notched specimens. The sample dimension is 14 mm × 2.8 mm × 3 mm (length × width × thickness) with a 1 mm sharp notch. 3-point bending test specimens without notch (14 mm × 2.8 mm × 2.5 mm) are used to measure the bending strength of the composites. Each specimen has 7-8 fibers and both tests had a same support span of 12 mm. The bending tests were performed using an Instron 3342 universal testing machine (Instron GmbH) with a displacement rate of 5 μm/s. During the tests, the force and displacement were measured and the tests continued until complete failure of the specimen. Two identical specimens of each

type of composites were prepared for each test. After mechanical testing, the microstructure of the fracture section is analyzed via SEM (LEO 982).

2.3 FEM analysis

The simulations were performed using the commercial software ABAQUS Standard 2021. A 2D plane strain pre-crack model under quasi-static bending load was analyzed by the XFEM implemented in this software. The geometric size of model is shown in Figure 2a where X and Y are the directions parallel and perpendicular to the fibers, respectively. The simplified 2D model is constructed to reduce the computational effort. The fibers in the weave are homogenized to a continuous layer which has a planar interface to the surrounding matrix (as shown in Figure2b). Therefore the area of the interface is not represented correctly. In this respect, this 2D model is only suitable to show some principal mechanism of the toughening and the absolute stress values or force-displacement relationships of this 2D model are not relevant.

The properties of tungsten matrix and tungsten fibers were chosen based on previous research [17,37] and some properties of the W matrix and W fiber used for modelling are shown in Table 1. The mechanical properties of the tungsten fiber after 2173 K annealing in Ref. [37] are used for modelling, because this temperature matches the FAST process of the fabrication. The interface between the fiber and matrix is modelled by a cohesive contact. The fracture properties of the Y_2O_3 interface was measured by a double cantilever beam (DCB) method. Figure 2d shows the geometry of the DCB sample which was prepared according to the process shown in Figure 2c. After the test, the mode-I strain energy release rate, G_{IC} is calculate by the following formula [38]:

$$G_{1C} = \frac{12P^2a^2\varphi}{B^2h^3E_{11}} \quad (1)$$

where P is the applied load, a is the current crack length, B and h are the width (2 mm) and half thickness (2.8 mm) of the DCB sample, respectively. E_{11} is the elastic modulus of W, 400 GPa. φ is a geometrical parameter related to the thickness, here $\varphi = 1$, because the interface is in the middle of the sample. Based on the tested load (29 N) and crack length (3.8 mm), the energy release rate used in the modelling can be calculated as $G_{1C} = 4.15$ J/m^2 according to equation (1). The calculated G_{1C} is the upper bound of the true value. The elastic modulus and strength of Y_2O_3 are 170 GPa and 54-83 MPa, respectively [39]. The median value of strength 70 MPa is used for the modelling.

Table 1. The properties of the W matrix and W fiber used for modelling.

	Matrix (W)	Fiber (W_f)
Elastic modulus, E (GPa)	400	400
Poisson's ratio, υ (-)	0.28	0.28
Ultimate strength, σ_I (MPa)	380	1968
Fracture energy, Γ (J/m^2)	114	360

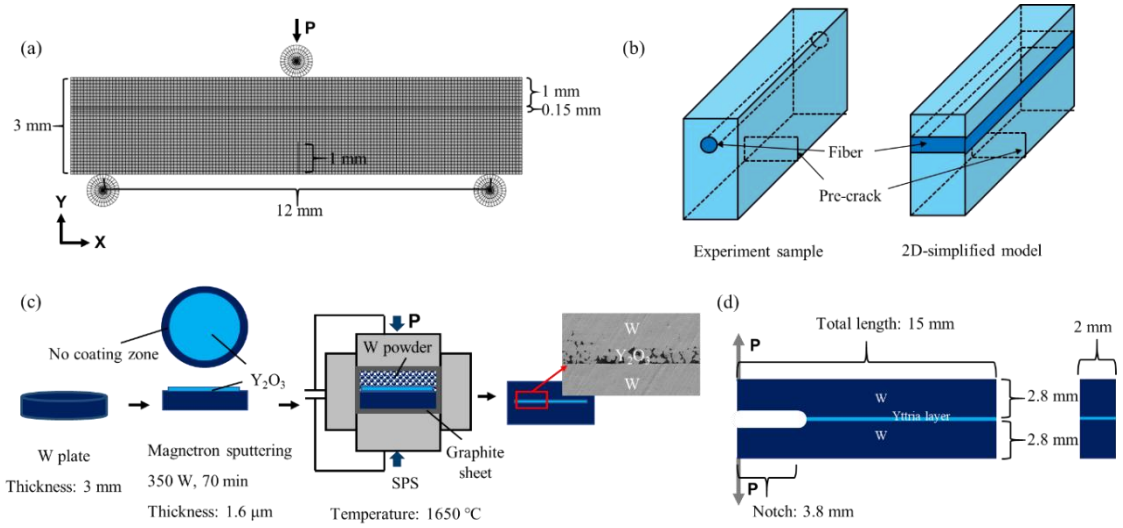

Figure 2. (a) Geometric diagram of 2D model for XFEM analysis; (b) The geometry of the experiment sample and 2D-simplified model; (c) Schematic diagram of the preparation process of the DCB sample; (d) Geometric diagram of DCB test sample.

3. Results

3.1 Microstructure of the W_f/W composites

Figure 3 shows the microstructure of the sintered W_f/W composites with Y_2O_3 interface (Figures 3a-c) and without interface (Figures 3d and 3e). As shown in Figures 3a-c, there is a clear interface layer between fiber and matrix. The interface is not continuous and the thickness of the Y_2O_3 region is about 8 μm, which is much thicker than the originally coated Y_2O_3 layer (≈1.6 μm). This reveals that the Y_2O_3 layer is destroyed during the FAST process and diffuses into the surrounding matrix, as it has been reported in [22]. Since the fiber is fully dense and remains unchanged during the FAST process, the Y_2O_3 interface in contact with the fiber surface shows little damage and maintains its continuity. However, on the matrix side, with the raw material being W powders (1200 mm^{-1}) whose specific surface area

of unit volume is 45 times larger than the fiber (26.7 mm^{-1}). Because the Joule effect is the main heating source during the FAST process, the large electrical resistance at the interface between W powders leads to high local temperature, which leads to the destruction of the structure of the Y_2O_3 layer. Moreover, there is a destruction caused by dielectric breakdown [40], as Y_2O_3 is electrically insulating. Therefore, the Y_2O_3 mainly got damaged and moved towards the matrix side, leading to the microstructure shown in Figures 3b and 3c. In Figures 3d and 3e, there is no clear boundary and the regions of fibers and matrix are difficult to distinguish. The lack of an interface layer leads to a direct contact between fibers and powders, thus forming a metallurgical W-W boundary during the sintering process, which is usually strong as the matrix.

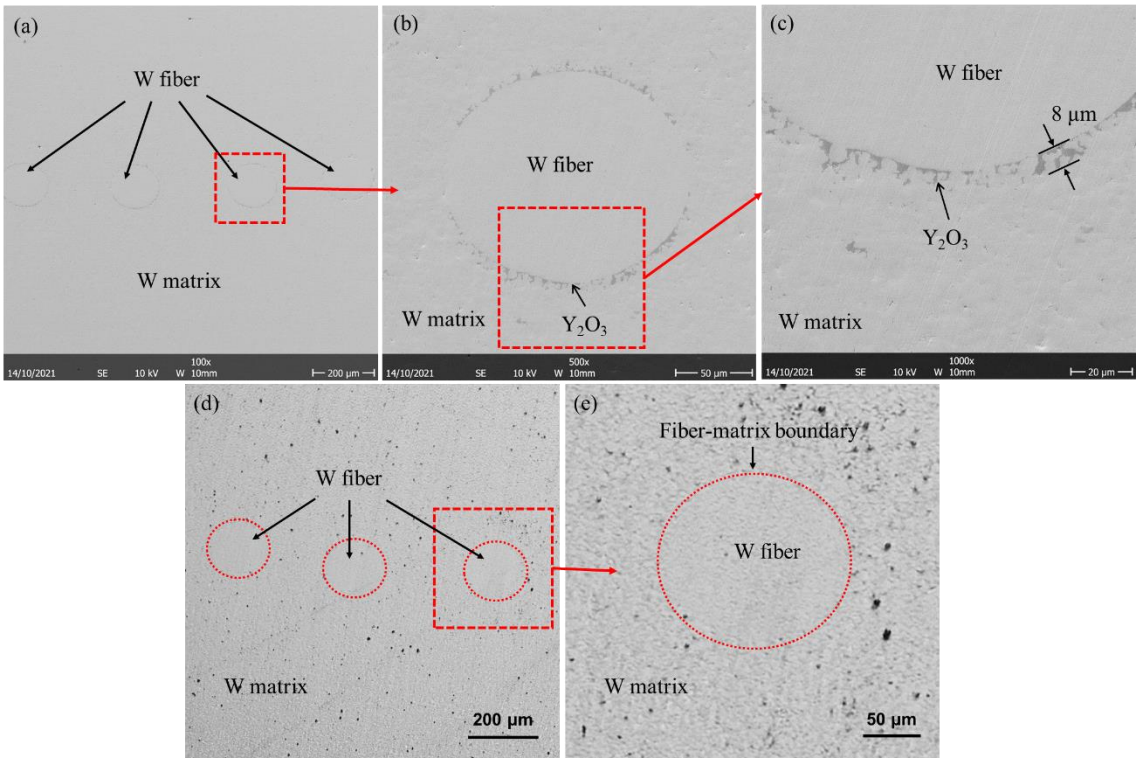

Figure 3. (a-c) Microstructure of the W_f/W composite with Y_2O_3 interface; (d, e) Microstructure of the W_f/W composite without Y_2O_3 interface.

In addition to the interface, the microstructure of fibers and matrix in the prepared W_f/W composites was analyzed. Figures 4a and 4b are SEM images of the fiber cross section prepared by FIB cut, which reveal the grain structure of the fibers for the sintered W_f/W composites with and without Y_2O_3 interface, respectively. The fibers have a columnar microstructure where the grain size along the fiber axis direction is much larger than that in the radial direction. The radial grain sizes of the fibers are measured by intercept method and their average values are 0.48 μm and 0.47 μm, respectively. According to these values, the fibers have similar grain sizes. It indicates that the Y_2O_3 interface has no effect or little effect on the microstructure of fibers during the FAST process as performed in this work. Meanwhile, the similar compactness and fracture microstructure shows that the interface has the same little influence on the microstructure of the matrix, that is the matrix of both composites has the same microstructure.

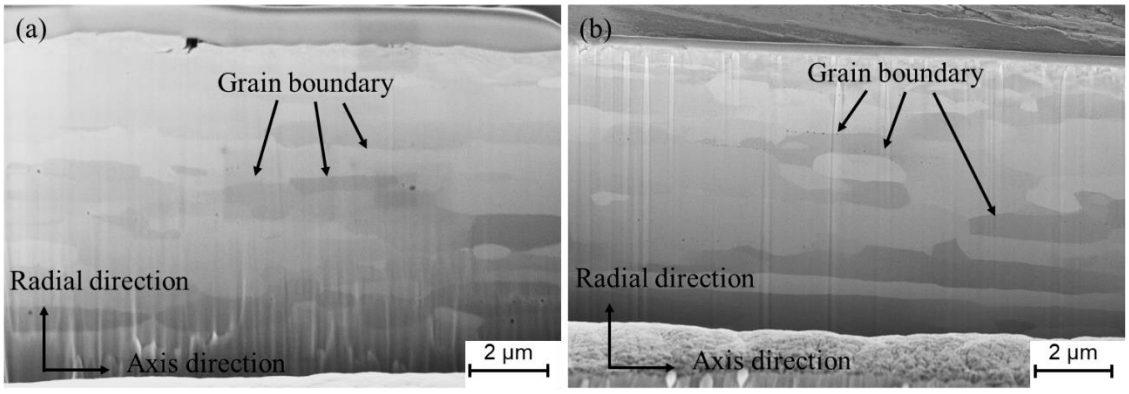

Figure 4. SEM images of the W fiber in different W_f/W composites prepared by FIB cut: (a) With Y_2O_3 interface; (b) Without Y_2O_3 interface.

3.2 Mechanical properties of the W_f/W composites

As part of this study, the flexural strength of the W_f/W composites was obtained by carrying out the 3-point bending test until the complete fracture of both matrix and fibers.

The calculated flexural strength of the samples without interface are 488 MPa and 504 MPa, and the values of the samples with interface are 559 MPa and >600 MPa (limited by the maximum force of the test machine 500 N). The results show that the strength of the composite with interface is higher than that without interface. In general, a weak interface may reduce the strength of composites [17], because the weak interface tends to be the crack initiation sites under loads. The interface strength in present work is sufficient to fully exploit to the strength of the W fibers. In contrast, because the strong boundary limits the plastic deformation of fibers, the strength advantage of fibers in the Wf/W composite without interface is limited. And both of them are higher than the pure W prepared through the same process, which is around 380 MPa [17]. The increase in flexural strength is mainly dependent on the high strength of the W fiber.

3.3 Fracture behavior of the W_f/W composites

Figure 5 shows the typical force-displacement curves of the notched samples for the 3-point bending test, where the red and blue lines are the test results of the samples with interface and without interface, respectively. Both curves have two peaks: while the occurrence of the first peaks is similar, the second peaks occur at different strains indicating different fracture behavior. The composite with interface layer (red curve) shows a larger fracture strain and a better pseudo-ductile behavior during the fracture process. The composite without interface layer (blue curve) has lower strain giving almost a brittle fracture. A detailed discussion will be given in the following section.

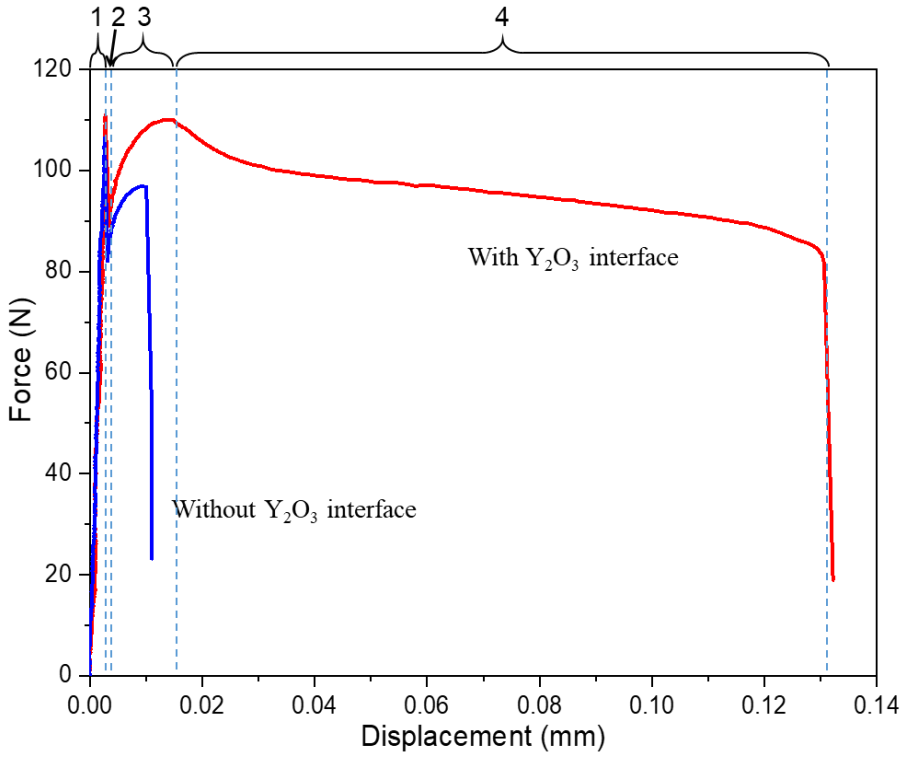

Figure 5. Force-Displacement curves of the single-layer long fiber reinforced W_f/W composites tested by 3-point bending.

In order to analyze the fracture mechanisms further, SEM was used to observe the fracture surface morphology. It is found in Figures 6 and 7 that the matrix fractured mainly in the intergranular fracture mode, which is a typical brittle fracture. However, the fibers have different fracture modes depending on the interface condition. All of the eight fibers in the composite with interface layer are ductile fracture, whereas all seven fibers in the composite without interface layer failed in brittle manner.

Figures 6a-c reveal the morphology of the fracture surface of fibers that failed in a ductile manner, which occurs in the composite with interface. There are a large number of obvious radial cracks on the fiber fracture surface [41]. The fiber cross-sectional area is significantly reduced. The original fiber diameter is about 150 μm, while the average diameter after

fracture is about 120 μm, and thus has decreased by ≈20%. This indicates that necking occurs during the fracture process. In addition, it can be observed that there is a significant interface de-bonding phenomenon between fibers and matrix, and there are many cracks in the region adjacent to the fibers. This phenomenon is due to the discontinuity of the Y_2O_3 layer on the interface, where some W particles have direct contact with fibers and the bonding strength is thus relatively high. During the fracture process, a de-bond crack is first generated and then propagate in the low-strength Y_2O_3 layer or the interface between the Y_2O_3 layer and fibers. The de-bonding will then propagate into the matrix where the Y_2O_3 shows a discontinuous distribution (as shown in Figure 3c). The positions where fibers and matrix are in direct contact has a higher strength, so cracks do not easily propagate, but propagate via the matrix near it. Thus, some broken matrix particles adhere onto the surface of fibers. Figure 6d illustrates the fracture process of the composite with interface. When a crack generates in the matrix and propagates to a fiber, the Y_2O_3 layer will be destroyed due to shear stress (shear lag model) [39,42]. It leads to a free surface area of the fiber (a region that is not constrained by the matrix), which in turn allows for the plastic deformation of the fiber [43]. As the load continues to increase, the fiber shows necking and eventually fractures completely, forming a fracture surface as shown in Figure 6a-c.

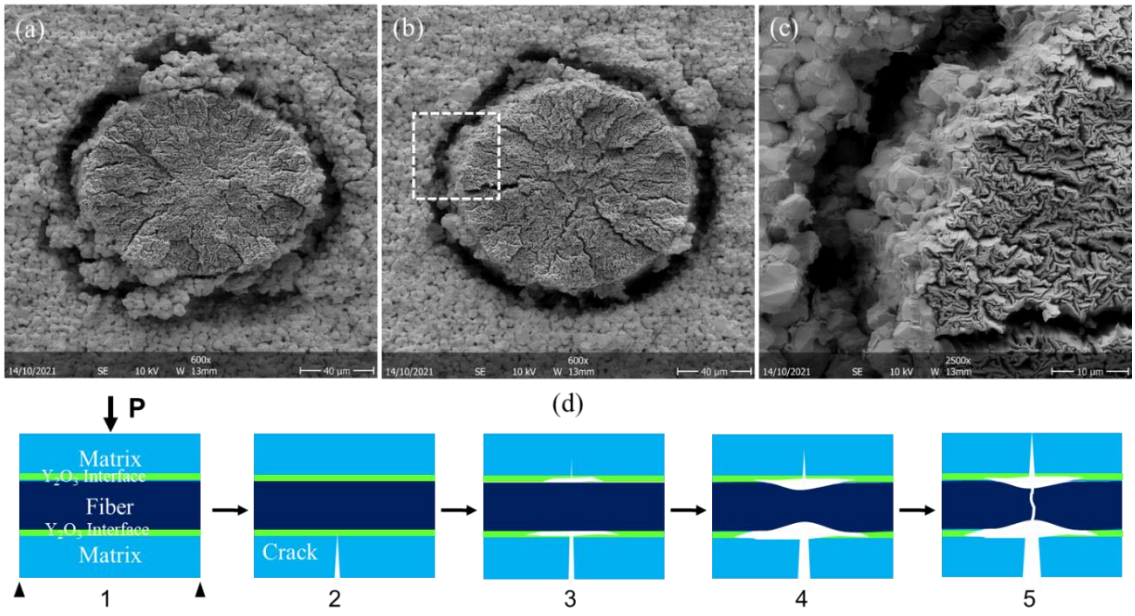

Figure 6. (a-c) The fracture microstructure of ductile fracture fibers (c is the enlarged image of the dotted region in b); (d) Diagrams of fracture process during the 3-point bending test: the sample with interface.

On the contrary, fibers in the composite without interface undergo complete brittle fracture without interface de-bonding or reduction of the fiber diameter, as shown in Figures 7a-c. During the fracture process, the fiber will suffer with a triaxial tensile stress (will be discussed also in the following section), because the bonding strength between fibers and matrix is too high to enable de-bonding. The fibers tend to fail brittle under this loading state [33] although it has the same plastic properties as those of the fibers in the composite with interface. The fracture process is as shown in Figure 7d.

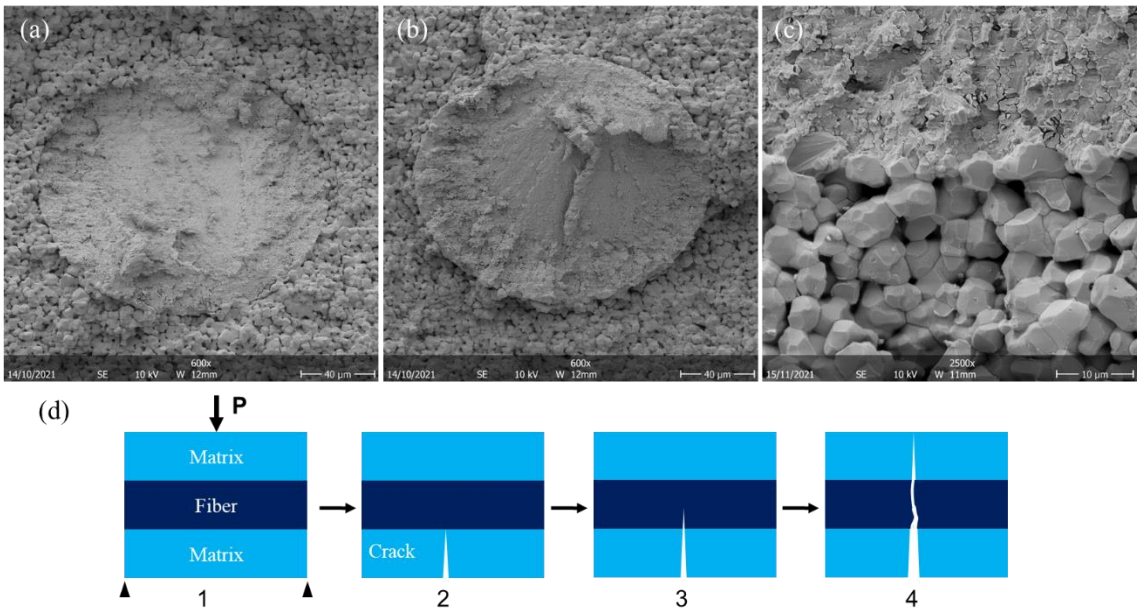

Figure 7. (a-c) The fracture microstructure of brittle fracture fibers; (d) Diagrams of fracture process during the 3-point bending test: the sample without interface.

3.4 FEM modelling results

In order to analyze the stress distribution of the composites with various fiber-matrix interface strength, notched 3-point bending tests were modelled through 2D finite element models incorporating the composites with various interface properties. Figure 8 illustrates the von Mises stress distribution of the composites with interface (with de-bonding capability) and without interface (perfectly bonded, no de-bonding capability) at different stages. As shown in Figures 8a1-f1, a stress concentration region is formed at the tip of the notch with the increase of the load (Figure 8b1). As the load continues to increase, a crack is generated at the tip of the notch and propagates steadily, with the interface starting to de-bond at the position of the highest stress (Figure 8c1, where the stress distribution in the fiber and the matrix starts to become discontinuous.). At that time, the crack propagates and is then stopped by the fiber, where the de-bonding area expands rapidly (Figures 8d1 and 8e1). As shown in

Figure 8d1, the interface de-bonding leads to a great difference of the stress on both sides of the interface between the fiber and matrix. Before the fiber fractures, cracks may already be generated at the matrix on the top side of the fiber (Figure 8e1). With the increase of loading, the fiber has a part of surface area without the constraint of matrix and mainly suffers tensile stress along its axial direction (Figure 8f1), which is conducive to its plastic deformation. In contrast, the composite without interface shows no interface de-bonding during the whole process (Figures 8a2-f2). The stress on both sides of the interface shows continuous distribution, which is much different from the stress distribution of the composite with interface. The crack also initiates at the notch top, and propagates through both the matrix and the fiber to the other side of the sample unhindered.

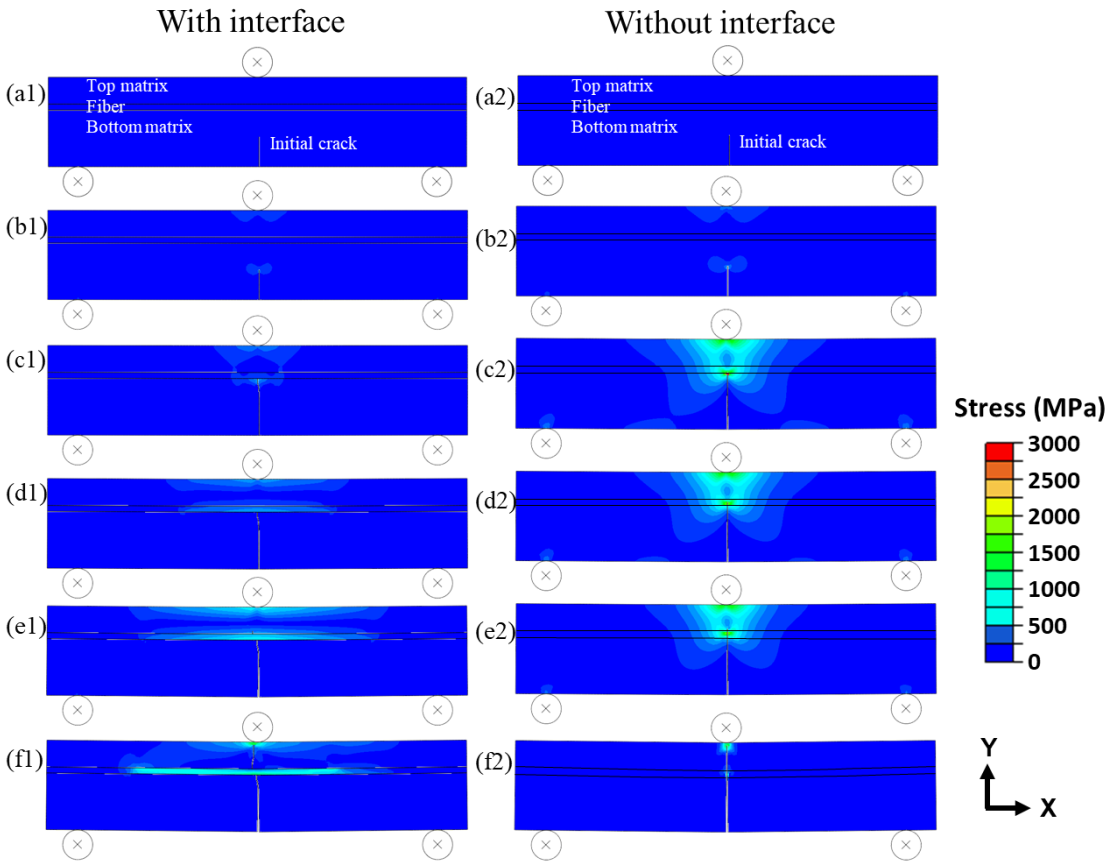

Figure 8. Distribution of von Mises stress of the fiber reinforced composites with and without interface.

As mentioned in Section 2.3, the matrix has been divided into two individual parts which are untouched with each other by the continuous fiber layer in present 2D model, while the fiber layer does not completely separate the top and bottom parts of the matrix in the real composite (as shown in Figure 2b). In the model with interface, a new crack generates in the top side matrix after the interface de-bonding (Figure 8e1). On the contrary, in the real composite, the crack in the bottom part of the matrix will propagate into the top matrix through the gaps of the fibers, which is a process of crack propagation rather than the generation of new cracks.

Figure 9 illustrates the directional stress condition of the composites with or without interface for different directions at the point of fiber cracking. The fiber with interface mainly suffers tensile stress in X direction (Figure 9a1), and the stress in Y direction (Figure 9a2) is small. The fiber without interface is continuous with the matrix, therefore stresses in both X and Y directions are present. (Figures 9b1 and 9b2). For the composite with interface, the de-bonding part of fiber only has the constraint along the fiber direction, and is free in other directions, so it just suffers the tensile stress in one direction. On the contrary, the fiber in the composite without interface is constrained in all directions, which is not conducive to its plastic behavior [44,45].

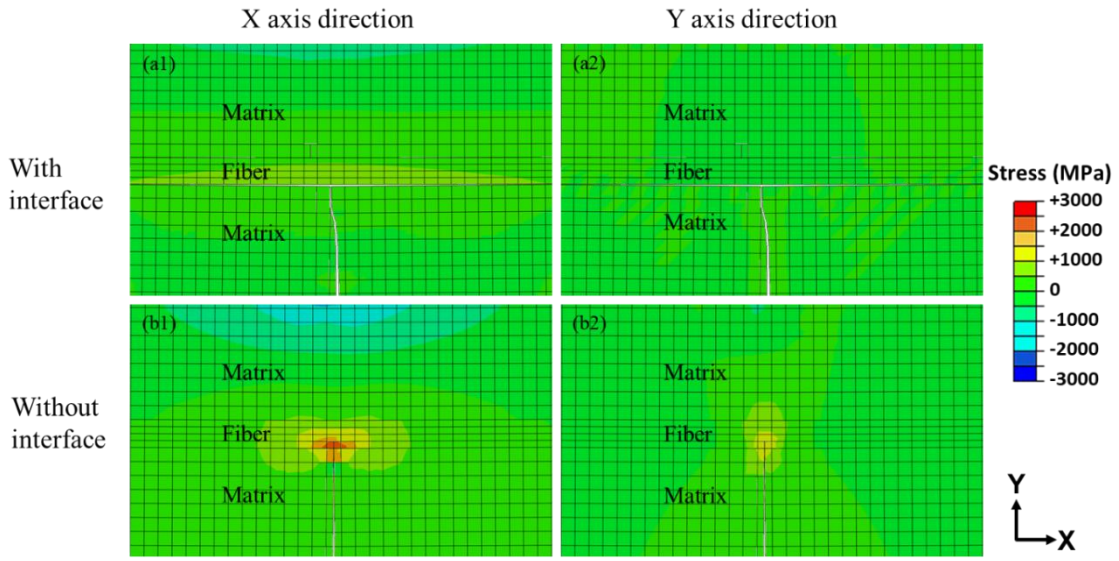

Figure 9. Stress distribution of the fiber in X axis direction and Y axis direction of the composites with and without interface, respectively. The layer of the fabric can be identified by its smaller element height. "+" indicates tensile stress (warm colours in the colour bar) and "-" indicates compressive stress (cool colours in the colour bar).

4. Discussion

As we interpret the combination of experimental results and FEM simulation, we can observe that there are several stages during the 3-point bending test process (as shown in Figure 5):

Stage 1: This stage is mainly based on the elastic deformation of the W matrix because as long as the fiber stress is below its yield stress the fiber has the same stiffness as the matrix. Moreover, there is only one layer of fibers in the composites, the volume fraction of the fiber is about 2.5%, which contributes little to it. At this stage, the stress is mainly on the matrix (before crack starting, as shown in Figures 8b1 and 8b2). The slopes of both curves are similar

and the maximum force values are very close, indicating that the matrix of the samples have similar elastic modulus and strength. This is also evidence that the interface has little effect on the properties of the matrix in this work.

Stage 2: After reaching the maximum force, a sudden drop of the load occurs, because the brittle W matrix reaches its maximum strength, cracks generate and extend rapidly until being stopped by fibers.

Stage 3: Due to the high strength and toughness of fibers as well as the geometry (The large aspect ratio and alignment perpendicular to crack.) [46], the propagation of cracks has been hindered by the fibers, thus the load increases again gradually. This process is mainly due to the elastic deformation and work hardening of the fibers. For these 3 stages, the two curves show a similar evolution process. However, the next stage shows different phenomena between these two curves.

Stage 4: For the blue curve, it is just a sudden drop of force after the peak. The red curve slowly decreases and keeps at about 90 N reaching a large displacement, about 0.1 mm (76.9% of the total displacement). And then a sudden drop occurs because of the sudden fracture of the fibers and the residual matrix on the top side of the fiber layer. As the fibers in both composites have the same microstructure and properties, we can postulate that the difference between the two curves is mainly driven by the interface layer.

For the sample with interface, the interface de-bonding is more likely to occur and followed by fiber deformation. The fracture surface of fibers with necking is a strong evidence for the plastic deformation of fibers (as shown in Figures 6a-c), the evolution of the fracture process is explained in Figure 6d. The simulation results in section 3.4 intuitively illustrate the failure process of the composite and show that interface de-bonding occurs

before the plastic deformation of the fiber. Although the model has a strong simplification and is hard for quantitative analysis, it shows the similar evolution trend with the experiment and works for qualitative analysis. At the same time, with the increasing de-bonding length, the fiber can be more plastically deformed, and the overall toughness of the composite is significantly improved as in [43]. While for the sample without interface, strong metallurgical bonding could be formed between the fiber and matrix. De-bonding is hard to occur between fibers and matrix. The crack propagation process between matrix and fiber is illustrated as Figure 7d, which is also demonstrated by the simulation results (Figures 8a2-f2). Although the fiber cannot show a large plastic deformation as that of the fibers in the composite with interface, there may be micro local plastic deformation to blunt the crack tip.

The energy dissipated during the sample fracture process can be regarded as the work done by the load:

$$Q = W = \int_0^{u_{max}} F \cdot du \tag{2}$$

Where, Q is the dissipated energy of sample fracture process, W is work done by the load, F and u are the value of loading force and displacement, respectively. And u_{max} is the maximum displacement when the sample totally fails. According to this equation, the dissipated energy can be roughly calculated by integrating the curves. In the present work, the curves can be divided into two parts: brittle fracture part (stage 1 and 2) and ductile fracture part (stage 3 and 4). Therefore, the equation (1) can be modified as:

$$Q = Q_b + Q_d = \int_0^{u_1} F \cdot du + \int_{u_1}^{u_{max}} F \cdot du \tag{3}$$

Q_b and Q_d are the dissipated energy of brittle fracture part (Corresponding to the Stage 1 and Stage 2 of the curves in Figure 5) and ductile fracture part (Corresponding to the Stage

3 and Stage 4 of the curves in Figure 5), respectively. u_1 is the displacement of the end of brittle fracture part, here means the end of stage 2 or the beginning of stage 3. The calculated values are shown in Table 2. The values in Table 2 reveal that the sample with Y_2O_3 interface (12.54 mJ) dissipates much more energy than the sample without interface (0.91 mJ). It is noteworthy that both of the samples have similar Q_b value of ≈0.2 mJ. While Q_d contributes 98.4% for the total dissipated energy of the sample with Y_2O_3 interface. This indicates that the existence of Y_2O_3 interface has a great impact on the toughness of the prepared W_f/W composites.

Table 2. Dissipated energy of the samples during fracture process.

Sample	Q (mJ)	Q_b (mJ)	Q_d (mJ)	Q_b%	Q_d%
With interface	12.54	0.20	12.34	1.6	98.4
Without interface	0.91	0.19	0.72	20.9	79.1

Considering the different mechanisms, Q also can be expressed as:

$$Q = Q_{matrix} + Q_{fiber} + Q_{de} \tag{4}$$

where, Q_{matrix} is the energy dissipation caused by the brittle fracture of W matrix, which is mainly caused by the crack initiation and almost equal to Q_b. The process of crack propagation in the brittle W matrix is instantaneous and leads to minimal energy dissipation (as shown in Figure 5). Q_{fiber} indicates the energy dissipated by fibers which is mainly contributed by plastic deformation of the fibers. Because the elastic modulus of tungsten is 400 GPa, the elastic strain energy has a fraction smaller than 1% and can be ignored in this work. Q_{de} is the dissipated energy by interface de-bonding which only exists in the W_f/W

composite with interface when de-bonding occurs.

It can be simply calculated by the equation:

$$Q_{de} = nA_{de}G_{1C} \tag{5}$$

where n is the number of fibers in test samples, the de-bonding area $A_{de} = \pi dl$, d and l are the diameter of fiber and de-bonding length, respectively. The energy release rate caused by interface de-bonding is $G_{1C} = 4.15$ J/m^2, the fiber has a diameter of 0.15 mm and there are 8 fibers in each test sample. Figure 10 reveals the microstructure of the necking fracture of the fiber, we can see that the necking deformation of the fiber occurred at the whole de-bonding area. As shown in Figure 10b, there is the end of de-bonding on the interface at the edge of the necking region of the fiber, the distance between the de-bonding end and the fracture surface of matrix is half of the total de-bonding length. The measured de-bonding length in Figure 10c is 96 μm. After the measurement and statistics of the de-bonding length of fibers, the average de-bonding length of the fibers in this study is 186 μm, which leads to a de-bonding area of $A_{de} = 0.088$ mm^2. Hence, the energy dissipation by de-bonding in the composite can be approximated as $Q_{de} = 8 \times 0.088\ \text{mm}^2 \times 4.15\ \text{J/m}^2 = 2.92 \times 10^{-3}$ mJ. It means that the dissipated energy by interface de-bonding only has a small contribution to the total amount of dissipated energy.

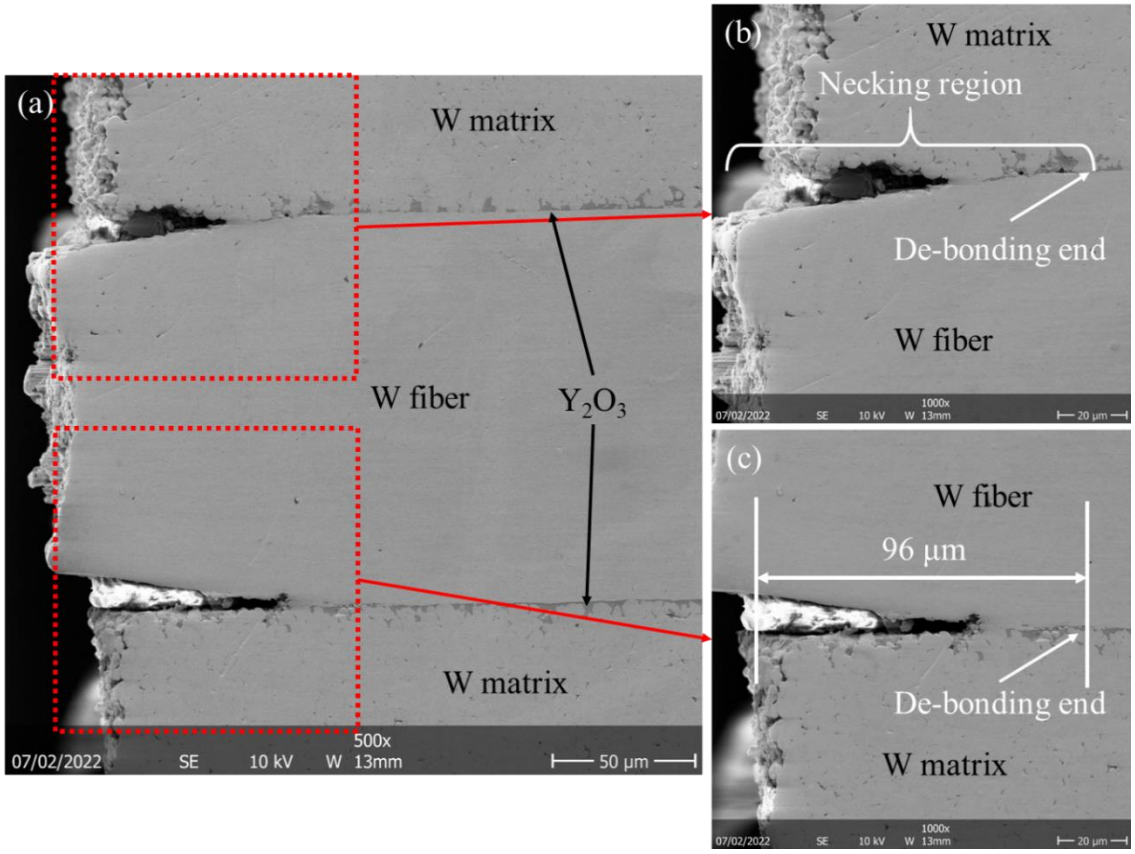

Figure 10. Microstructure of necking fracture fiber in the W_f/W composite with interface.

Hence, the energy dissipation by fiber:

$$Q_{fiber} = Q - Q_b - Q_{de} \approx Q_d \tag{6}$$

For the composite with interface, $Q_{fiber}^{with\ interface} \approx 12.34$ mJ, which contributes 98.4% to the total fracture energy dissipation and per fiber is ≈1.54 mJ (there are 8 fibers in the test sample). While the energy dissipation of the composite without interface owing to fibers is $Q_{fiber}^{without\ interface} \approx 0.72$ mJ, only has the fraction of 79.1% and the contribution of each fiber is ≈0.09 mJ, because there is no plastic deformation in it. Hence, the contribution of fibers on fracture energy dissipation in the composite with interface is higher than that in the composite without interface.

Because the deformation lengthen is equal to the de-bonding length of 186 μm, the plastic deformation energy per unit volume of the fiber in the composite with interface in this work is:

$$\omega_{f,pl} = \frac{Q_{fiber}^{with\ interface}}{8\pi r_f^2 l} = 0.47\ \mathrm{J/mm^3} \quad (7)$$

where r_f is the radius of the fiber. The value is close to the value reported in Ref. [41] (0.56 J/mm^3, the fiber shows the deformation with macroscopic necking and localized deformation and with a de-bonding length of 250 μm), and it is higher than the reported value of the constraint necking deformation of the W fiber (0.19 J/mm^3, with a de-bonding length of 66 μm) and the value of the no constraint necking process (0.093 J/mm^3) in Ref. [43]. The energy dissipation by plastic deformation is strongly dependent on the de-bonding length, i.e. on the strength of interface. A weaker interface leads to a higher de-bonding length, higher energy dissipation by plastic deformation but would also need a larger crack opening to dissipate the energy. Ref. [41] gives an idea de-bonding length of approximately 250 μm which would be sufficient to allow a full plastic deformation (a process with the highest energy dissipation). It indicates that interface de-bonding is an important and necessary factor to facilitate the plastic deformation of fibers, and the interface produced by the method of this work would be sufficient to realize the toughening mechanism of plastic deformation of fibers.

5. Conclusion

Single-layer long fiber reinforced W_f/W composites were prepared by FAST process. The mechanism leading to extrinsic toughening were linked to the interfacial de-bonding occurring during the 3-point bending tests performed where the fiber contributes with its high

strength and plasticity, showing obvious plastic deformation and fracture with necking only for the composite with Y_2O_3 interface. The toughening mechanisms of the composite with interface are interface de-bonding and plastic deformation of fibers. The contribution of each mechanism is calculated here. During the fracture process, the dissipation of energy is mainly contributed by plastic deformation of fibers (98%), and interface de-bonding is a prerequisite of the plastic deformation of fibers. However, for the composite without Y_2O_3 interface, the strong W-W metallurgical interface limits the plastic behavior of the tungsten fibers. Thus, the composites fail in a rather brittle behavior. This is in line with the findings of other brittle matrix composites.

In future work, multi-layer fiber reinforced W_f/W composites will be prepared via powder metallurgy, and more quantitative tests and numerical simulation methods will be applied for the further investigation of the toughening mechanism of fiber reinforced composites and the contribution of each mechanism.

Acknowledgements

This work has been carried out within the framework of the EUROfusion Consortium, funded by the European Union via the Euratom Research and Training Programme (Grant Agreement No 101052200 - EUROfusion). Rui Shu is financially supported by China Scholarship Council (CSC) with No. 202007000034. Views and opinions expressed are however those of the author(s) only and do not necessarily reflect those of the European Union or the European Commission. Neither the European Union nor the European Commission can be held responsible for them.

References

[1] V. Philipps, Tungsten as material for plasma-facing components in fusion devices, J. Nucl. Mater. 415 (2011) S2. https://doi.org/10.1016/j.jnucmat.2011.01.110.

[2] J.W. Coenen, Fusion Materials Development at Forschungszentrum Jülich, Adv. Eng. Mater. 22 (2020) 1-15. https://doi.org/10.1002/adem.201901376.

[3] J.W. Coenen, Y. Mao, S. Sistla, A. V. Müller, G. Pintsuk, M. Wirtz, J. Riesch, T. Hoeschen, A. Terra, J.H. You, H. Greuner, A. Kreter, C. Broeckmann, R. Neu, C. Linsmeier, Materials development for new high heat-flux component mock-ups for DEMO, Fusion Eng. Des. 146 (2019) 1431-1436. https://doi.org/10.1016/j.fusengdes.2019.02.098.

[4] Y.H. Zhang, W.Z. Han, Mechanism of brittle-to-ductile transition in tungsten under small-punch testing, Acta Mater. 220 (2021) 117332. https://doi.org/10.1016/J.ACTAMAT.2021.117332.

[5] X.F. Xie, Z.M. Xie, R. Liu, Q.F. Fang, C.S. Liu, W.Z. Han, X. Wu, Hierarchical microstructures enabled excellent low-temperature strength-ductility synergy in bulk pure tungsten, Acta Mater. 228 (2022) 117765. https://doi.org/10.1016/J.ACTAMAT.2022.117765.

[6] S. Nogami, S. Watanabe, J. Reiser, M. Rieth, S. Sickinger, A. Hasegawa, A review of impact properties of tungsten materials, Fusion Eng. Des. 135 (2018) 196-203. https://doi.org/10.1016/j.fusengdes.2018.08.001.

[7] C. Ren, Z.Z. Fang, M. Koopman, B. Butler, J. Paramore, S. Middlemas, Methods for improving ductility of tungsten - A review, Int. J. Refract. Met. Hard Mater. 75 (2018) 170-183. https://doi.org/10.1016/j.ijrmhm.2018.04.012.

[8] R.W. Steinbrech, Toughening mechanisms for ceramic materials, J. Eur. Ceram. Soc. 10 (1992) 131-142. https://doi.org/10.1016/0955-2219(92)90026-A.

[9] S. Chen, W.Q. Li, L. Zhang, H.M. Fu, Z.K. Li, Z.W. Zhu, H. Li, H.W. Zhang, A.M. Wang, Y.D. Wang, H.F. Zhang, Dynamic compressive mechanical properties of the spiral tungsten wire reinforced Zr-based bulk metallic glass composites, Compos. Part B Eng. 199 (2020). https://doi.org/10.1016/j.compositesb.2020.108219.

[10] L.W. Yang, J.Y. Wang, H.T. Liu, R. Jiang, H.F. Cheng, Sol-gel temperature dependent ductile-to-brittle transition of aluminosilicate fiber reinforced silica matrix composite, Compos. Part B Eng. 119 (2017) 79-89. https://doi.org/10.1016/j.compositesb.2017.03.043.

[11] C. Linsmeier, M. Rieth, J. Aktaa, T. Chikada, A. Hoffmann, J. Hoffmann, A. Houben, H. Kurishita, X. Jin, M. Li, A. Litnovsky, S. Matsuo, A. Von Müller, V. Nikolic, T. Palacios, R. Pippan, D. Qu, J. Reiser, J. Riesch, T. Shikama, R. Stieglitz, T. Weber, S. Wurster, J.H. You, Z. Zhou, Development of advanced high heat flux and plasma-facing materials, Nucl. Fusion. 57 (2017). https://doi.org/10.1088/1741-4326/aa6f71.

[12] J. Du, T. Höschen, M. Rasinski, J.H. You, Shear debonding behavior of a carbon-coated interface in a tungsten fiber-reinforced tungsten matrix composite, J. Nucl. Mater. 417 (2011) 472-476. https://doi.org/10.1016/j.jnucmat.2010.12.254.

[13] H. Gietl, A. V. Müller, J.W. Coenen, M. Decius, D. Ewert, T. Höschen, P. Huber, M. Milwich, J. Riesch, R. Neu, Textile preforms for tungsten fibre-reinforced composites, J. Compos. Mater. 52 (2018) 3875-3884. https://doi.org/10.1177/0021998318771149.

[14] J.W. Coenen, M. Treitz, H. Gietl, P. Huber, T. Hoeschen, L. Raumann, D. Schwalenberg, Y. Mao, J. Riesch, A. Terra, C. Broeckmann, O. Guillon, C. Linsmeier, R. Neu, The use of tungsten yarns in the production for Wf/W, Phys. Scr. T171 (2020) 014061. https://doi.org/10.1088/1402-4896/ab6096.

[15] H. Gietl, S. Olbrich, J. Riesch, G. Holzner, T. Höschen, J.W. Coenen, R. Neu, Estimation of the fracture toughness of tungsten fibre-reinforced tungsten composites, Eng. Fract. Mech. 232 (2020) 107011. https://doi.org/10.1016/j.engfracmech.2020.107011.

[16] Y. Jiang, L.H. Zhang, Q.F. Fang, T. Zhang, X.P. Wang, T. Hao, C.S. Liu, Toughness enhancement of tungsten reinforced with short tungsten fibres, Mater. Sci. Eng. A. 690 (2017) 208-213. https://doi.org/10.1016/j.msea.2017.02.106.

[17] Y. Mao, J.W. Coenen, J. Riesch, S. Sistla, J. Almanstötter, B. Jasper, A. Terra, T. Höschen, H. Gietl, C. Linsmeier, C. Broeckmann, Influence of the interface strength on the mechanical properties of discontinuous tungsten fiber-reinforced tungsten composites produced by field assisted sintering technology, Compos. Part A Appl. Sci. Manuf. 107 (2018) 342-353. https://doi.org/10.1016/j.compositesa.2018.01.022.

[18] J.W. Coenen, Y. Mao, S. Sistla, J. Riesch, T. Hoeschen, C. Broeckmann, R. Neu, C. Linsmeier, Improved pseudo-ductile behavior of powder metallurgical tungsten short fiber-reinforced tungsten (Wf/W), Nucl. Mater. Energy. 15 (2018) 214-219. https://doi.org/10.1016/j.nme.2018.05.001.

[19] J. Riesh, M. Aumann, J.W. Coenen, H. Gietl, G. Holzner, T. Höschen, P. Huber, M. Li, C. Linsmeier, R. Neu, Chemically deposited tungsten fibre-reinforced tungsten-The way to a mock-up for divertor applications, Nucl. Mater. Energy. 9 (2016) 75-

83. https://doi.org/10.1016/j.nme.2016.03.005.

[20] H. Gietl, J. Riesch, J.W. Coenen, T. Höschen, C. Linsmeier, R. Neu, Tensile deformation behavior of tungsten fibre-reinforced tungsten composite specimens in as-fabricated state, Fusion Eng. Des. 124 (2017) 396-400. https://doi.org/10.1016/j.fusengdes.2017.02.054.

[21] J. Riesch, J.Y. Buffiere, T. Höschen, M. Scheel, C. Linsmeier, J.H. You, Crack bridging in as-fabricated and embrittled tungsten single fibre-reinforced tungsten composites shown by a novel in-situ high energy synchrotron tomography bending test, Nucl. Mater. Energy. 15 (2018) 1-12. https://doi.org/10.1016/j.nme.2018.03.007.

[22] Y. Mao, J.W. Coenen, J. Riesch, S. Sistla, J. Almanstötter, B. Jasper, A. Terra, T. Höschen, H. Gietl, M. Bram, J. Gonzalez-Julian, C. Linsmeier, C. Broeckmann, Development and characterization of powder metallurgically produced discontinuous tungsten fiber reinforced tungsten composites, Phys. Scr. T170 (2017) 014005. https://doi.org/10.1088/0031-8949/2017/T170/014005.

[23] E. Njuhovic, M. Bräu, F. Wolff-Fabris, K. Starzynski, V. Altstädt, Identification of interface failure mechanisms of metallized glass fibre reinforced composites using acoustic emission analysis, Compos. Part B Eng. 66 (2014) 443-452. https://doi.org/10.1016/j.compositesb.2014.06.018.

[24] C.J. Lissenden, Fiber-matrix interfacial constitutive relations for metal matrix composites, Compos. Part B Eng. 30 (1999) 267-278. https://doi.org/10.1016/S1359-8368(98)00062-6.

[25] S. Khandelwal, K.Y. Rhee, Recent advances in basalt-fiber-reinforced composites:

Tailoring the fiber-matrix interface, Compos. Part B Eng. 192 (2020) 108011. https://doi.org/10.1016/j.compositesb.2020.108011.

[26] J.P. Singh, D. Singh, M. Sutaria, Ceramic composites: roles of fiber and interface, Compos. Part A Appl. Sci. Manuf. 30 (1999) 445-450. https://doi.org/10.1016/S1359-835X(98)00133-X.

[27] K. Cui, Y. Zhang, T. Fu, J. Wang, X. Zhang, Toughening mechanism of mullite matrix composites: A review, Coatings. 10 (2020). https://doi.org/10.3390/coatings10070672.

[28] F.W. Zok, C.G. Levi, Mechanical Properties of Porous-Matrix Ceramic Composites, Adv. Eng. Mater. 3 (2001) 15-23. https://doi.org/10.1002/1527-2648(200101)3:1/2<15::AID-ADEM15>3.0.CO;2-A.

[29] Y. Mao, J.W. Coenen, J. Riesch, S. Sistla, J. Almanstötter, J. Reiser, A. Terra, C. Chen, Y. Wu, L. Raumann, T. Höschen, H. Gietl, R. Neu, C. Linsmeier, C. Broeckmann, Fracture behavior of random distributed short tungsten fiber-reinforced tungsten composites, Nucl. Fusion. 59 (2019) 1-28. https://doi.org/10.1088/1741-4326/ab25b0.

[30] Y. Mao, J.W. Coenen, J. Riesch, S. Sistla, C. Chen, Y. Wu, L. Raumann, R. Neu, C. Linsmeier, C. Broeckmann, Spark plasma sintering produced W-fiber-reinforced tungsten composites, Spark Plasma Sinter. Mater. Adv. Process. Appl. (2019) 239-261. https://doi.org/10.1007/978-3-030-05327-7.

[31] K. Balaji Thattaiparthasarathy, S. Pillay, H. Ning, U.K. Vaidya, Process simulation, design and manufacturing of a long fiber thermoplastic composite for mass transit application, Compos. Part A Appl. Sci. Manuf. 39 (2008) 1512-1521.

https://doi.org/10.1016/J.COMPOSITESA.2008.05.017.

[32] L.H. Zhang, Y. Jiang, Q.F. Fang, T. Zhang, X.P. Wang, C.S. Liu, Toughness and microstructure of tungsten fibre net-reinforced tungsten composite produced by spark plasma sintering, Mater. Sci. Eng. A. 659 (2016) 29-36. https://doi.org/10.1016/j.msea.2016.02.034.

[33] V. Laws, The efficiency of fibrous reinforcement of brittle matrices, J. Phys. D. Appl. Phys. 4 (1971) 1737-1746. https://doi.org/10.1088/0022-3727/4/11/318.

[34] J. Zhu, Y. Zhu, W. Shen, Y. Wang, J. Han, G. Tian, P. Lei, B. Dai, Growth and characterization of yttrium oxide films by reactive magnetron sputtering, Thin Solid Films. 519 (2011) 4894-4898. https://doi.org/10.1016/J.TSF.2011.01.049.

[35] Z. Dong, N. Liu, Z. Ma, C. Liu, Q. Guo, Y. Liu, Preparation of ultra-fine grain W-Y2O3 alloy by an improved wet chemical method and two-step spark plasma sintering, J. Alloys Compd. 695 (2017) 2969-2973. https://doi.org/10.1016/j.jallcom.2016.11.364.

[36] Y. Mao, J. Engels, A. Houben, M. Rasinski, J. Steffens, A. Terra, C. Linsmeier, J.W. Coenen, The influence of annealing on yttrium oxide thin film deposited by reactive magnetron sputtering: Process and microstructure, Nucl. Mater. Energy. 10 (2017) 1-8. https://doi.org/10.1016/j.nme.2016.12.031.

[37] J. Riesch, Y. Han, J. Almanstötter, J.W. Coenen, T. Höschen, B. Jasper, P. Zhao, C. Linsmeier, R. Neu, Development of tungsten fibre-reinforced tungsten composites towards their use in DEMO - Potassium doped tungsten wire, Phys. Scr. T167 (2016) 14006. https://doi.org/10.1088/0031-8949/T167/1/014006.

[38] R.S. Kumar, Crack-growth resistance behavior of mode-I delamination in ceramic

matrix composites, Acta Mater. 131 (2017) 511-522. https://doi.org/10.1016/j.actamat.2017.04.012.

[39] M. Satou, T. Yamakawa, A. Hasegawa, K. Abe, Evaluation of interface strength between metal and ceramics to be utilized for development of fusion reactor components, J. Nucl. Mater. 386-388 (2009) 689-691. https://doi.org/10.1016/j.jnucmat.2008.12.280.

[40] C.S. Bonifacio, T.B. Holland, K. Van Benthem, Time-dependent dielectric breakdown of surface oxides during electric-field-assisted sintering, Acta Mater. 63 (2014) 140-149. https://doi.org/10.1016/j.actamat.2013.10.018.

[41] J. Riesch, J. Almanstötter, J.W. Coenen, M. Fuhr, H. Gietl, Y. Han, T. Höschen, C. Linsmeier, N. Travitzky, P. Zhao, R. Neu, Properties of drawn W wire used as high performance fibre in tungsten fibre-reinforced tungsten composite, IOP Conf. Ser. Mater. Sci. Eng. 139 (2016) 012043. https://doi.org/10.1088/1757-899X/139/1/012043.

[42] L.B. Greszczuk, Theoretical Studies of the Mechanics of the Fiber-Matrix Interface in Composites, in: Interfaces Compos. Int., (1969) 42-58. https://doi.org/10.1520/stp44699s.

[43] J. Riesch, J.Y. Buffiere, T. Höschen, M. Di Michiel, M. Scheel, C. Linsmeier, J.H. You, In situ synchrotron tomography estimation of toughening effect by semi-ductile fibre reinforcement in a tungsten-fibre-reinforced tungsten composite system, Acta Mater. 61 (2013) 7060-7071. https://doi.org/10.1016/j.actamat.2013.07.035.

[44] M. Brünig, D. Brenner, S. Gerke, Stress state dependence of ductile damage and fracture behavior: Experiments and numerical simulations, Eng. Fract. Mech. 141

(2015) 152-169. https://doi.org/10.1016/J.ENGFRACMECH.2015.05.022.

[45] Y. Liu, L. Kang, H. Ge, Experimental and numerical study on ductile fracture of structural steels under different stress states, J. Constr. Steel Res. 158 (2019) 381-404. https://doi.org/10.1016/J.JCSR.2019.04.001.

[46] J. Riesch, A. Feichtmayer, M. Fuhr, J. Almanstötter, J.W. Coenen, H. Gietl, T. Höschen, C. Linsmeier, R. Neu, Tensile behaviour of drawn tungsten wire used in tungsten fibre-reinforced tungsten composites, Phys. Scr. T170 (2017) 014032. https://doi.org/10.1088/1402-4896/aa891d.